JOURNAL OF SPACECRAFT AND ROCKETS
Vol. 30, No. 2, March–April 1993

Computer Particle Simulation of High-Voltage Solar Array Arcing Onset

Mengu Cho* and Daniel E. Hastings†
Massachusetts Institute of Technology, Cambridge, Massachusetts 02139

The operation of a high-voltage solar array in low Earth orbit may cause arcing on the negatively biased parts of a solar array. This sets a practical limit on the operational voltage of solar arrays.This paper is the extension of three earlier works[1-3] regarding high-voltage solar array arcing. The onset of arcing is reproduced by self-consistent computer simulations to verify the arcing onset model developed in the earlier work. It is shown that neutral gas is desorbed from the dielectric surface forming a localized neutral cloud over the surface, and the arcing onset occurs as the gas breakdown at a parameter *pd* (pressure times distance) much smaller than the Paschen minimum. Analytical expressions for the prebreakdown electron currents and the neutral densities are also derived and used to obtain a parametric formula of the breakdown condition. Arcing rates are calculated including the breakdown condition of the desorbed neutral gas. The theory is compared to the Japanese Space Flyer Unit High-Voltage Solar Array ground experiment and shown to give a reasonable explanation for data relating the arcing rate to the solar array temperature.

Nomenclature

A = $1.54 \times 10^{-6} \times 10^{4.52\phi_w^{-1/2}}/\phi_w$, A/V^2
B = $6.53 \times 10^9 \phi_w^{1.5}$, V/m
C^+ = field enhancement factor induced by ion current
$\bar{c}$ = mean speed of gas, m/s
d = thickness of dielectric material $d_1 + d_2$, m
d_1 = thickness of coverglass, m
d_2 = thickness of adhesive, m
E = electric field, V/m
$E_{c.o.}$ = initial conductor (cathode) electric field, V/m
E_d = desorption energy, eV
E_i = electron incident energy, eV
$E_{\max}$ = electron incident energy for maximum secondary electron yield, eV
E_{se} = secondary electron emission energy, eV
E_{se1} = electron incident energy to give secondary electron yield unity, eV
E_x = electric field parallel to dielectric side surface, V/m
E_y = electric field perpendicular to dielectric side surface, V/m
I = total current, A
I_x = current per unit length in the direction parallel to dielectric side surface, A/m
I_y = current per unit length in the direction perpendicular to dielectric side surface, A/m
j_e = incident electron current density to dielectric surface, A/m^2
j_e^* = quasisteady incident electron current density to dielectric surface, A/m^2
j_{e0} = prebreakdown current density from conductor (cathode) before ionization begins, A/m^2
j_{ec} = enhanced field electron emission current density from conductor surface, A/m^2
j_{ec}^* = quasisteady current density due to negative space charge, A/m^2
j_i = ion current density to conductor due to ionization of neutral, A/m^2
k_1^0 = desorption rate coefficient, s^{-1}
m = particle mass, kg
N_n = number of gas particles adsorbed per unit area, m^{-2}
N_{no} = adsorbed neutral surface density for monolayer coverage, m^{-2}
n_n = neutral density, m^{-3}
n_{na} = ambient neutral density, m^{-3}
n_{nc} = critical neutral density for arcing onset, m^{-3}
p = pressure, Torr
q = particle charge, C
Q_{EID} = electron impact desorption cross section, m^{-2}
S_{FN} = emission area at metal-dielectric interface, m^2
S_{real} = emission area at dielectric-vacuum interface, m^2
s = sticking probability of neutral particle to dielectric surface
T = temperature, K
T_n = neutral temperature, K
T_s = surface temperature, K
V = bias voltage, V
V_{ad} = $V\{d_2/[\epsilon_{d_2}/\epsilon_{d_1})d_1 + d_2]\}$ voltage between the triple junction and the coverglass/adhesive interface, V
v_o = secondary electron emission speed, m/s
v_{ex} = velocity of electron in x direction over dielectric surface, m/s
α = electron emission polar angle
α_{ion} = Townsend Ionization coefficient, cm
β = field enhancement factor
Γ_{EID} = electron impact desorption flux, m^{-2} s^{-1}
Γ_{TSD} = thermal desorption flux, m^{-2} s^{-1}
γ_{ee} = secondary electron yield
$\gamma_{\max}$ = maximum secondary electron yield at normal incidence
ϵ_{d_1} = relative dielectric constant of coverglass
ϵ_{d_2} = relative dielectric constant of adhesive
σ = charge density per unit area, C/m^2
σ_{ion} = ionization collision cross section, m^2
σ_- = electron density per unit area over dielectric side surface, C/m^2
τ_{chrg} = charging time of dielectric surface, s
ϕ_s = dielectric surface potential, V
ϕ_w = conductor surface work function, eV
θ_i = electron incident angle
φ = electron emission azimuthal angle
ζ = fraction of returning ions which contributes to the field enhancement at the emission site

Received Jan. 18, 1992; revision received Sept. 16, 1992; accepted for publication Sept. 26, 1992.

*Research Assistant, Dept. of Aeronautics and Astronautics; currently, Research Associate, Graduate School of Science and Technology, Kobe University, Kobe 657, Japan. Member AIAA.

†Associate Professor, Dept. of Aeronautics and Astronautics. Member AIAA.

I. Introduction

THE use of high power in future space missions calls for high-voltage power generation and transmission. Photovoltaic power generation is the most likely candidate for the near future missions because of its high reliability and superior power density up to 100 kW. The operation of high-voltage solar arrays in low Earth orbit, however, causes serious environmental interactions with the surrounding space plasma. Arcing on the negatively biased part of the solar array is one of the most serious problems, which sets a practical limit on the operational voltage of the solar array. It causes electromagnetic noise and may also damage the solar cells. In one space experiment arcing was observed to occur at a voltage as low as -200 V.[4]

A review of the laboratory experiments with respect to arcing has been given in Ref. 5. The critical elements for an arc discharge have been found to be the presence of dielectric material (such as the coverglass or adhesive) in the vicinity of the highly biased conductor or semiconductor where both are in contact with the space plasma. Another critical element seems to be the presence of a precursor electron current from the conductor. Arcing in the experiments has been defined as a sudden increase in the current much larger than the ambient current collection and typically lasting a few microseconds. The arcs are highly localized phenomena which have been observed to occur at the edge of the coverglass. They are sometimes but not always associated with the interconnector.[6]

In recent theoretical work, Cho and Hastings[1] studied the charging of the region near the plasma, dielectric, and conductor interface. The study was based on the two previous theoretical models by Parks et al.[7] and Hastings et al.[5] The model system which they studied is shown in Fig. 1. It consists of dielectric material placed on a negatively biased conductor in a plasma environment. For a solar array, the dielectric material corresponds to the coverglass and adhesive and the conductor corresponds to the interconnect. The solar cell itself is neglected because it is a semiconductor with a voltage drop across it of at most 1–2 V. The important terminologies regarding the region of interest are the following: *dielectric side surface,* the surface perpendicular to the conductor surface; *dielectric front surface,* the surface parallel to the conductor; *triple junction,* the point where the conductor, the dielectric, and the vacuum meet.

In Ref. 1, it was shown that a strong electric field $E \sim V/d$ appeared near the triple junction as the result of charging of the coverglass front surface by ambient ions. If there was an enhanced field electron emission (EFEE) site on the conductor surface as proposed by Parks et al.,[7] electrons were emitted profusely and could charge the dielectric side surface positively by emitting more than one secondary electron upon their impact. The charging of the side surface enhanced the electric field at the triple junction further and developed very rapidly because of the strong exponential dependence of the current on the electric field. We call this charging process EFEE charging.

Figure 2 shows the time variation of the total emission current calculated by the space-charge-free orbit integration scheme developed in Ref. 1. For the initial conditions, we choose the state where the dielectric front surface is charged to $\phi_s = 0$ and the side surface is uncharged, that is, the potential

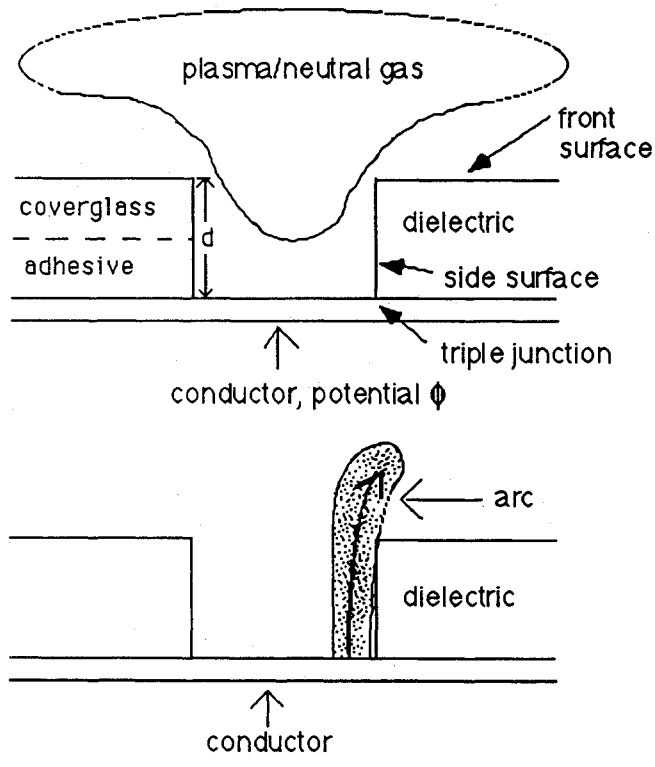

Fig. 1 Model system of high-voltage solar array—plasma interaction.

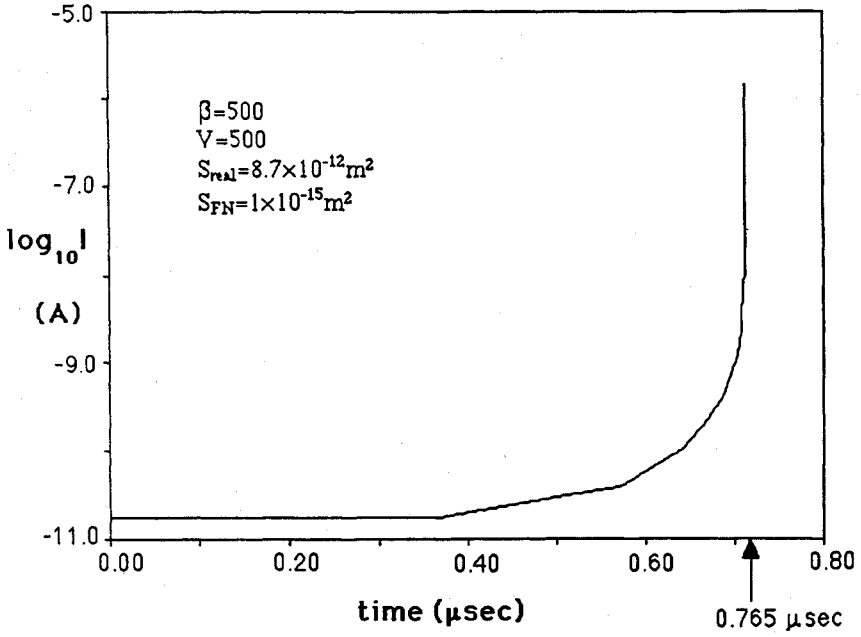

Fig. 2 Electron emission current from conductor surface calculated by space-charge-free orbit integration scheme.

changes linearly from 0 to V. The other parameters are discussed later in Sec. II. As the EFEE charging proceeds, we see a rapid increase of the emission current up to five orders of magnitude larger than its initial value.The calculation in Fig. 2 has been terminated at $t = 0.765$ μs when the emission current density has exceeded 10% of the space-charge-limited current density. In Sec. II, we see how this current is limited by the electron space charge.

While the emission current increases, there is strong electron incident current to the dielectric side surface which can desorb neutral gas from the surface. In Ref. 1, the density of the neutral cloud was roughly estimated to be as dense as 10^{23} m^{-3}. The characteristic scale length of the present problem is the dielectric thickness d, which is a few hundred microns. Multiplying the pressure p of the desorbed neutral gas by the length d, the product pd is less than the Paschen minimum (for example see Ref. 8), and can be categorized as "semivacuum" where the ionization collision mean free path is longer than d. In another recent work,[2] Cho and Hastings studied the semivacuum breakdown mechanism and showed breakdown voltages of the order of hundreds of volts are possible even in this range of pd. They studied a hypothesis proposed by Boyle et al.[9] which attributed the breakdown to the EFEE current from the cathode and the feedback effect provided by the field enhancement due to positive ion space charge at the cathode surface. In this paper, we call this breakdown model the BKG (Boyle, Kisliuk, and Germer) model. Analytical expressions for the breakdown conditions for a simple one-dimensional gap filled with argon were provided and compared with the numerical results obtained by a Monte Carlo-Particle in Cell (MC-PIC) code which included charged particle-neutral collisions.

In Ref. 3, the results of Ref. 1 were used to calculate arcing rates of the Japanese Space Flyer Unit (SFU) High-Voltage Solar Array (HVSA) ground experiment based on the assumption that arcing occurs whenever a current runaway occurs. In Ref. 3, the breakdown condition of the neutral cloud was not considered and the arcing rates calculated were regarded as upper bounds on the real arcing rates. Because the breakdown condition was not included in Ref. 3, the theoretical results could not give a quantitative explanation for the dependence of the arcing rates on the array temperature.

There are two major aims in the present paper. One is to reproduce the onset of arcing by two-dimensional MC-PIC simulations with the self-consistent neutral density and verify the arcing onset model developed in the earlier work. The other is to obtain an analytical formula for the arcing onset condition. We develop an analysis of the prebreakdown electron current densities and apply the result to the two-dimensional semivacuum breakdown condition which is modified from the one-dimensional result of Ref. 2. The arcing rates are calculated with the inclusion of the breakdown condition to compare the theory to the available experimental data for the arc rate dependence on the array temperature.

In Sec. II, we first extend the study on the prebreakdown process of Ref. 1 to include the effect of negative space charge and follow the motion of neutral particles desorbed from the surface. We show that the rapid current increase shown in Fig. 2 is not sufficient to explain the arcing onset. An analysis is made of the space-charge-limited emission current density from the conductor and the electron incident current density to the dielectric side surface. It is also shown that the gas breakdown at less than 1000 V must be due to a mechanism other than a Townsend discharge because the parameter pd is smaller than the Paschen minimum. In Sec. III, we simulate the gas breakdown of the neutral cloud by the MC-PIC code and show the onset of arcing is explained by the BKG model. We extend the one-dimensional breakdown condition obtained in Ref. 2 to the present two-dimensional system and obtain a parametric formula for the breakdown condition and calculate the critical electron impact desorption (EID) yield for given sets of parameters. In Sec. IV, the critical condition is applied to the calculation of the arcing rate developed in Ref. 3. The results are compared with the SFU-HVSA ground experimental data. Finally, in Sec. V, we conclude the paper by summarizing the new results and suggest future work.

II. Prebreakdown Processes of Arcing Onset

A. Computational Model

For the computational system, we use the parameters of SFU-HVSA ground experiments.[3] The SFU-HVSA flight experiment, which is due to fly in 1994, plans to use a conventional set of 2 × 4 cm silicon solar cells with exposed interconnectors between the cells and generate photovoltaic power with a voltage of up to a high voltage of 280 V. The thicknesses of the coverglass and adhesive are $d_1 = 153$ μm and $d_2 = 37$ μm, respectively. Throughout this work, we neglect the effects of the magnetic field because the electron gyro-radius is much longer than these lengths. The dielectric constants are $\epsilon_{d_1} = 7.3$ for the coverglass, and $\epsilon_{d_2} = 2.7$ for the adhesive. These parameters represent typical values of these conventional solar cells.

For the secondary electron yield, we assume the following formula[10]:

$$\gamma_{ee} = \gamma_{\max} \frac{E_i}{E_{\max}} \exp\left(2 - 2\sqrt{\frac{E_i}{E_{\max}}}\right) \exp[2(1 - \cos\theta_i)] \qquad (1)$$

We choose $\gamma_{\max} = 2.4$ and $E_{\max} = 400$ eV both for the coverglass and the adhesive. For the secondary electron emission, we assume a Gaussian distribution for the energy with 2 eV temperature and a cosine distribution for the emission angle. The interconnector is modeled by a gap whose width is 0.63 mm and each coverglass has a length of 20.17 mm between interconnectors. The computational grid system is shown in Fig. 3. Typically, the computational domain was 64 × 60 grid cells simulating a real space of either 30 mm × 20.8 mm or 90 mm × 20.8 mm.The boundary conditions are Dirichlet conditions in the x direction and periodic conditions in the y direction. One simulation particle represents typically 100 to 10,000 real particles. The artificial charge to mass ratio for the ambient ions is set to be the real one for argon, i.e., $(q_i/m_i)/|q_e/m_e| = 1.373 \times 10^{-5}$. Argon is chosen as the background ion because it is used in the ground experiments for the SFU.[3] In the ionosphere the background plasma species is mostly atomic oxygen. The difference of the ion species will give rise to a different shape for the sheath surrounding the interconnector. However, the potential structure near the triple junction is little affected by the ambient ion species.

The EFEE current density from an emission site is given by[3]

$$j_{ec} = A'\beta^2 E^2 \exp[-(B/\beta E)] \qquad (2)$$

We assume an electric field enhancement due to a thin dielectric layer. The electric field E in Eq. (2) is the field at the dielectric-vacuum interface of the layer. It is enhanced by a factor of β at the metal-dielectric interface. The factor A' in Eq. (2) is given by[3]

$$A' = A\frac{S_{FN}}{S_{real}} = \frac{1.54 \times 10^{-6} 10^{4.52\sqrt{\phi_w}}}{\phi_w} \frac{S_{FN}}{S_{real}}, \quad \mathrm{A/V^2} \qquad (3)$$

where the factor S_{FN}/S_{real} has been introduced to account for the negative space charge effect near the emission site.[3] The areas S_{FN} and S_{real} have the physical meanings of the emission area at the metal-dielectric and dielectric-vacuum interfaces of the thin dielectric layer, respectively.[3] The constants A and B are derived from the basic Fowler-Nordheim equation.[11] The surface work function is assumed to be 4.5 eV. The emission site is located on the conductor surface which is also the boundary $x = 0$. For simplicity, we assume a uniform field enhancement factor β over the emission site. Outside the emission site, the field enhancement factor is assumed to be unity.

In the present paper, we use different computer schemes for the different stage of the arcing onset process. Figure 4 summarizes the relation of the numerical schemes used in this

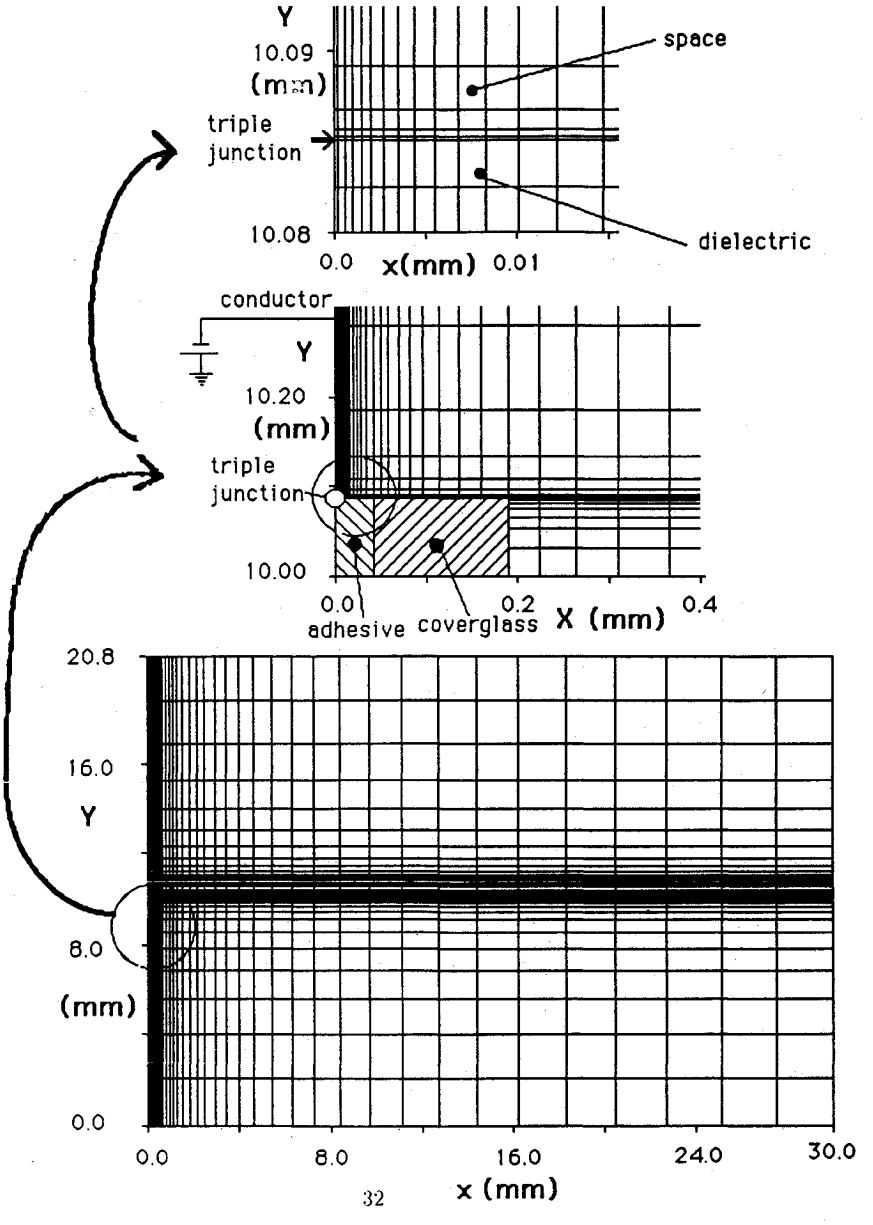

Fig. 3 Typical computational grid structure.

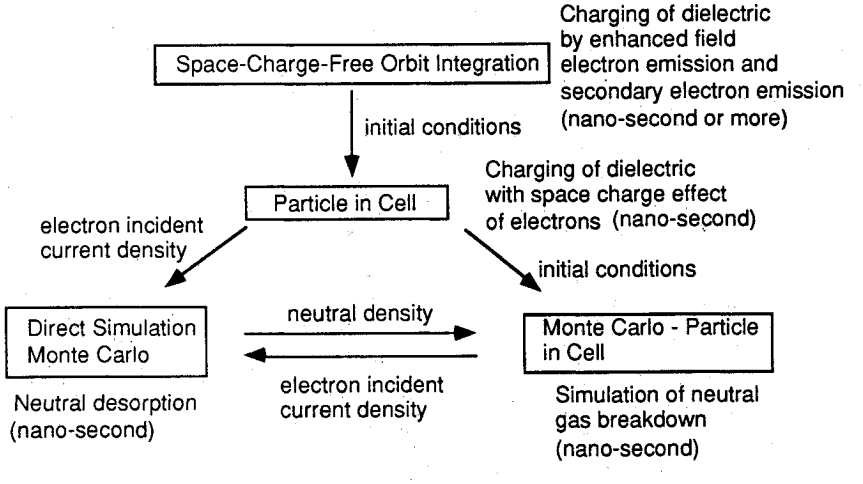

Fig. 4 Relation of computer schemes used in the paper. Dominant physical phenomena and their time scales are also shown.

paper. They share the computational grid shown in Fig. 3 and the initial conditions are passed from one to another. Discussions to justify the application of each numerical scheme are given where the properties of each code are discussed.

B. Space-Charge-Limitation of EFEE Emission Current

First, we consider how the EFEE emission current is space charge limited after it shows a runaway characteristic as shown in Fig. 2. We use the Particle in Cell (PIC) code because it gives the particle motion self-consistently with the space charge density and it is especially good for the small time scale (nanosecond) and the short length scale (millimeter) of the present problem. The details of the PIC code are given in Ref. 1. As a test case, we use the same parameters as the ones used for the example shown in Fig. 2. We use the final state of the orbit integration simulation as the initial conditions for the PIC simulation. The bias voltage is -500 V and we assume that an emission site with the field enhancement factor $\beta = 500$ is located on the conductor surface in contact with the triple junction. The effect of the location of emission site on the conductor is discussed in Ref. 3 in terms of the arcing rate. As typical values, we took[3] $S_{real} \simeq 10^{-11}$ m^2 and $S_{FN} = 10^{-15}$ m^2. The grid system shown in Fig. 3 gives the real emission site area $S_{real} = 8.7 \times 10^{-12}$ m^2, by assigning five grid cells in the y direction to the emission site.

We show the time variation of the total emission current calculated by the PIC code in Fig. 5. In the first 0.2 ns, we still see the rapid increase of the emission current due to the positive surface charge of the side surface. However, the current increase is limited when the negative space charge of electrons, which now lie extensively over the side surface, becomes comparable to the positive surface charge.

In Figs. 6a and b, we show the electric potential and electron positions near the triple junction, where the time corresponds to the time in Fig. 5. In Fig. 6a, electron space charge is negligible near the triple junction and strong discontinuities of the electric potential are present at the dielectric side surface due to the positive surface charge acquired by the side surface during the EFEE charging. As a result, the electric field near the triple junction is highly enhanced. At 0.25 ns later, a sheet of electrons covers the side surface, as shown in Fig. 6b; this is a result of the high electron current density from the conductor. This sheet of negative charge cancels the positive charge stored on the side surface, so the electric field on the side surface is decreased.

This decrease of electric field results in the decrease of electron emission current from the conductor. Therefore, once the electric field at the conductor decreases, the negative space charge over the dielectric surface also begins to decrease. By this time, however, most of the dielectric side surface charge density has reached a steady state by having a secondary electron yield of unity. Therefore, the decrease of negative space charge and emission current should stop when the amount of negative space charge balances the positive side-surface charge. Then, the emission current becomes quasi-steady as shown in Fig. 5. After reaching the quasisteady state, the emission current decreases very gradually as the electrons discharge the front surface. However, this discharge process over the front surface proceeds very slowly because electrons spread very widely over the front surface.

C. Analytical Expression of Prebreakdown Current Densities

We now formulate the analytical expressions for the space charge limited current densities. We consider a sheet of electrons hopping along the dielectric side surface. We take the x axis parallel to the side surface and the y axis perpendicular to the side surface. The current parallel to the surface is given by

$$I_x = \sigma_- v_{ex} = j_{ec}^* \sqrt{S_{real}} \tag{4}$$

A similar formulation of electron sheet current is found in the literature of vacuum surface flashover (see Ref. 12). In Ref. 13, the lateral (z direction) expansion of the electrons over the dielectric side surface was estimated to be about 10 μm. Since we consider the emission site area of $S_{real} \sim 10^{-11}$ m^2, we can neglect the lateral expansion of electrons. In Eq. (4), the current I_x is equal to the total EFEE current $j_{ec}^* \sqrt{S_{real}}$ because of current continuity.

Taking the average over the distribution function of the secondary electron emission given by

$$f(v, \alpha, \varphi)\, dv\, d\Omega = (1/\pi)[\delta(v - v_o)]\cos\alpha \sin\alpha\, dv\, d\alpha\, d\varphi \tag{5}$$

we obtain the electron velocity v_{ex} as

$$v_{ex} = \langle v_x \rangle = \frac{2}{3}\sqrt{\frac{2eE_{se}}{m_e}}\left(\frac{E_x}{E_y}\right) \tag{6}$$

Here, for simplicity, the fields E_x and E_y have been assumed uniform and monoenergetic emission with $eE_{se} = \frac{1}{2} m_e v_o^2$ has

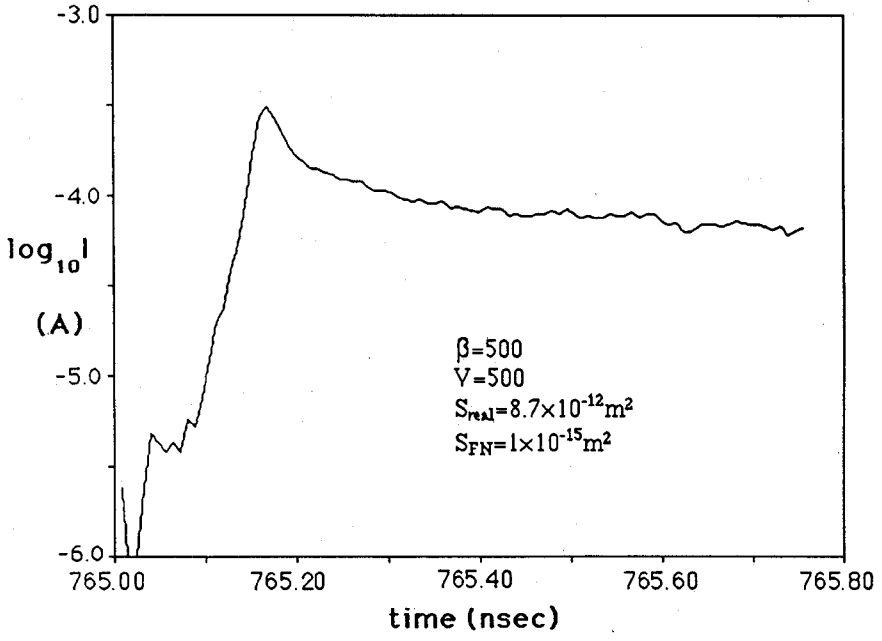

Fig. 5 Electron emission current from conductor surface calculated by PIC code following the result in Fig. 2.

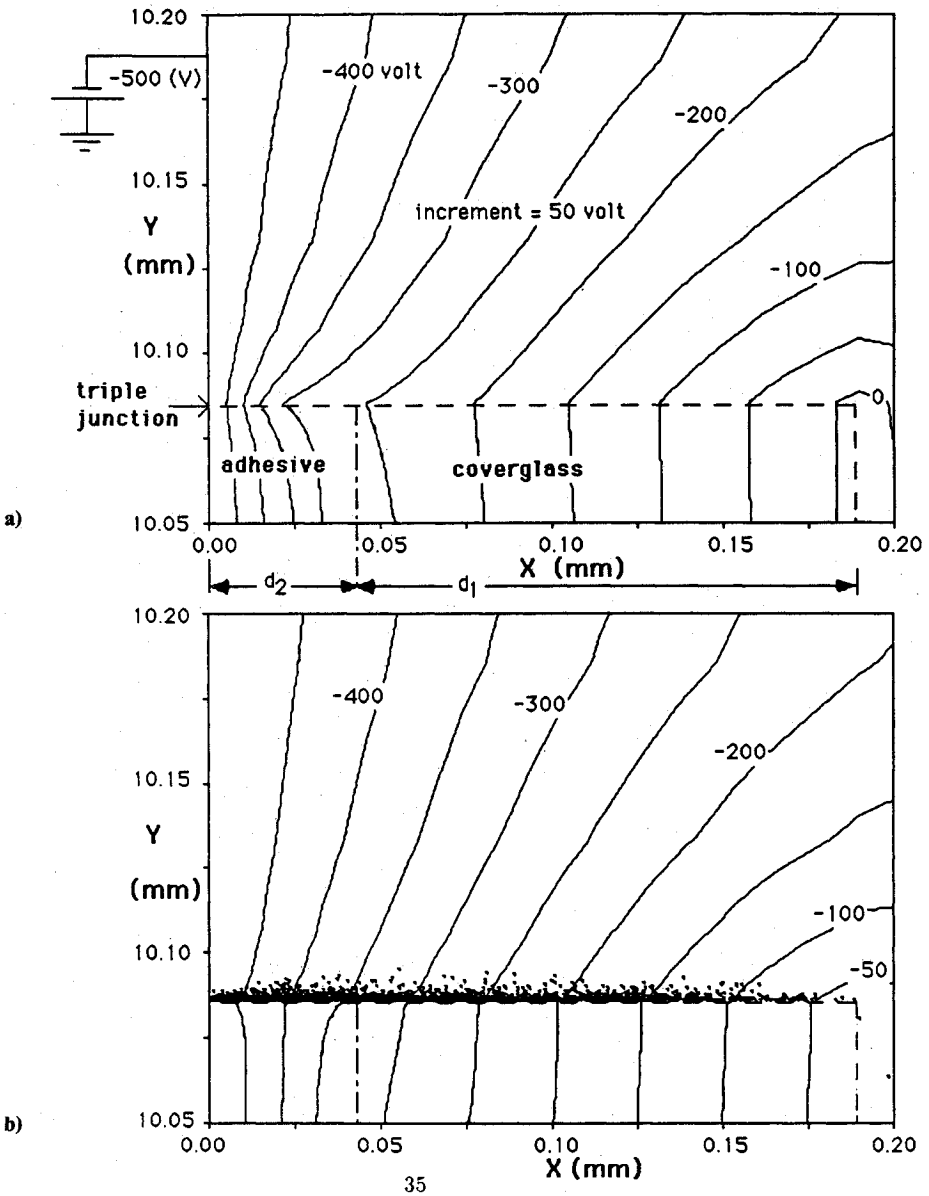

35

Fig. 6 Electric potential and electron position: a) t = 765.00 ns; and b) t = 765.25 ns. Black dots in the figure represents the electron positions.

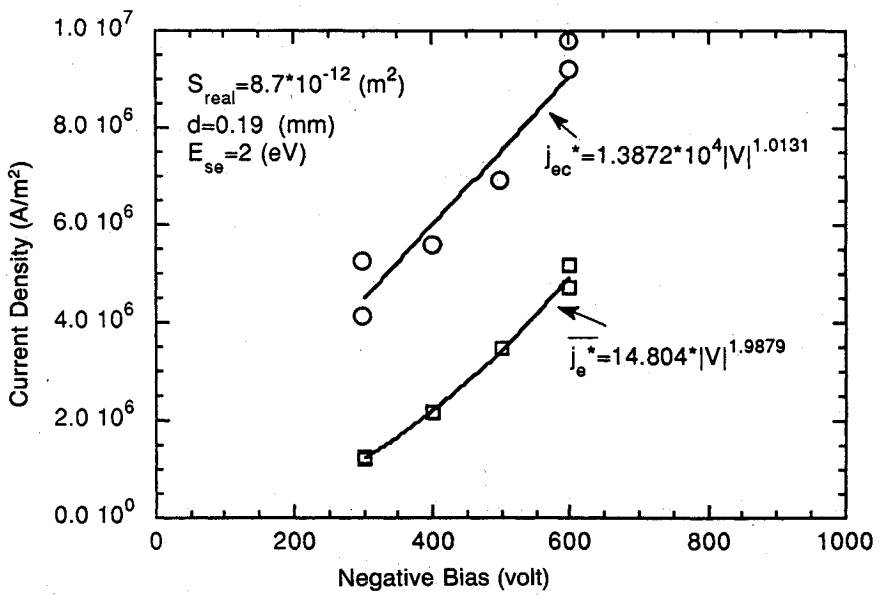

Fig. 7 Negative space-charge-limited current j_{ec}^*: quasisteady EFEE current density from conductor surface $\overline{j_e^*}$: quasisteady incident electron current density to dielectric side surface.

been assumed. The magnitude of E_x is approximated by the bias voltage $|V|$ as $E_x \simeq |V|/d$.

The negative space charge density σ_- is comparable to the dielectric surface charge density σ. The surface charge density σ is approximated by

$$\sigma/2\epsilon_o \simeq E_y \tag{7}$$

Equating σ_- and σ, and substituting Eq. (6) into Eq. (4), the negative space-charge-limited current density j_{ec}^* is given by

$$j_{ec}^* = \frac{4}{3}\epsilon_o \sqrt{\frac{2e}{m_e}} \frac{\sqrt{E_{se}}}{\sqrt{S_{real}}d} |V| \tag{8}$$

Figure 7 shows the current density j_{ec}^* calculated by the PIC code for various sets of V and β. The least square fit to the computations gives a linear dependence of j_{ec}^* on V as $j_{ec}^* = 1.39 \times 10^4 |V|$ A/m^2 with V in volts. Substituting for the parameters used for the PIC simulations, $S_{real} = 8.7 \times 10^{-12}$ m^2, $d = 190$ μm, and $E_{se} = 2$ eV into the analytical expression Eq. (8), we obtain $j_{ec}^* = 1.77 \times 10^4 |V|$. Despite the simple assumptions used to obtain Eq. (8), these values agree very well with the numerical results shown in Fig. 7. Using the simulation results to correct the numerical factors 4/3 in Eq. (8), the current densities is now written as

$$j_{ec}^* = 1.05\epsilon_o \sqrt{\frac{2e}{m_e}} \frac{\sqrt{E_{se}}}{\sqrt{S_{real}}d} |V|, \quad \text{A/m}^2 \tag{9}$$

It should be noted that the current density j_{ec}^* is independent of β.

Although the quasisteady emission current j_{ec}^* is a significant amount of current compared to the initial value, it is still too low to be the arcing current observed in experiments. Without any neutral desorption and the succeeding breakdown of the gas, the current simply relaxes to zero without arcing. For the arcing to be initiated, there must be a high density of neutral gas present in the region, which is produced by the electron impact desorption.

In the quasi-steady state, there is an intense electron incident current to the side surface. We formulate the expression for the incident electron current density. From current continuity, the incident current per unit length in the y direction I_y is equal to the electron current parallel to the dielectric surface I_x. The incident electron current density j_e^* is given by dividing the current I_y by the distance which the electron travels during one hop over the surface x_{hop}. Then the current density incident on the dielectric surface j_e^* is written as

$$j_e^* = \frac{I_y}{x_{hop}} = \frac{I_x}{x_{hop}} = \frac{j_{ec}^* \sqrt{S_{real}}}{x_{hop}} \tag{10}$$

We assume that the secondary electron yield from the dielectric side surface has already reached unity with the lower electron incident energy of the two energies which give the secondary yield of unity. Then, the hopping distance must satisfy $x_{hop} = E_{se1}/E_x$. Substituting this into Eq. (10) and using Eq. (8), straightforward algebra gives the incident current density j_e^* by

$$j_e^* = \frac{4}{3}\epsilon_o \sqrt{\frac{2e}{m_e}} \frac{\sqrt{E_{se}}}{E_{se1}d^2} |V|^2 \tag{11}$$

Figure 7 also shows the average electron incident current density to the side surface, $\overline{j_e^*}$, which is calculated by the PIC simulations for various sets of V and β. The current $\overline{j_e^*}$ is defined by

$$\overline{j_e^*} \equiv \frac{\int_0^{d_1+d_2} j_e^*(x)\, dx}{d_1 + d_2}$$

The numerical results are fitted very well by the square of the bias voltage V as $\overline{j_e^*} = 14.8 |V|^2$ with V in volts.

For the emission velocities and the emission probability distribution function given by Eq. (5) with $E_{se} = 2$ eV, $E_{max} = 400$ eV, and $\gamma_{max} = 2.4$, the incident energy $E_i = 7.6$ eV at an incident angle $\theta_i = 71.2$ deg has a secondary yield of unity. Then, the premultiplier in front of $|V|^2$ in Eq. (11) is given by $j_e^* = 36V^2$. Using the simulation results to correct the numerical factors 4/3 in Eq. (11), the current density is now written as

$$j_e^* = 0.52\epsilon_o \sqrt{\frac{2e}{m_e}} \frac{\sqrt{E_{se}}}{E_{se1}d^2} |V|^2, \quad \text{A/m}^2 \tag{12}$$

with E_{se}, E_{se1} in electron volts and $|V|$ in volts.

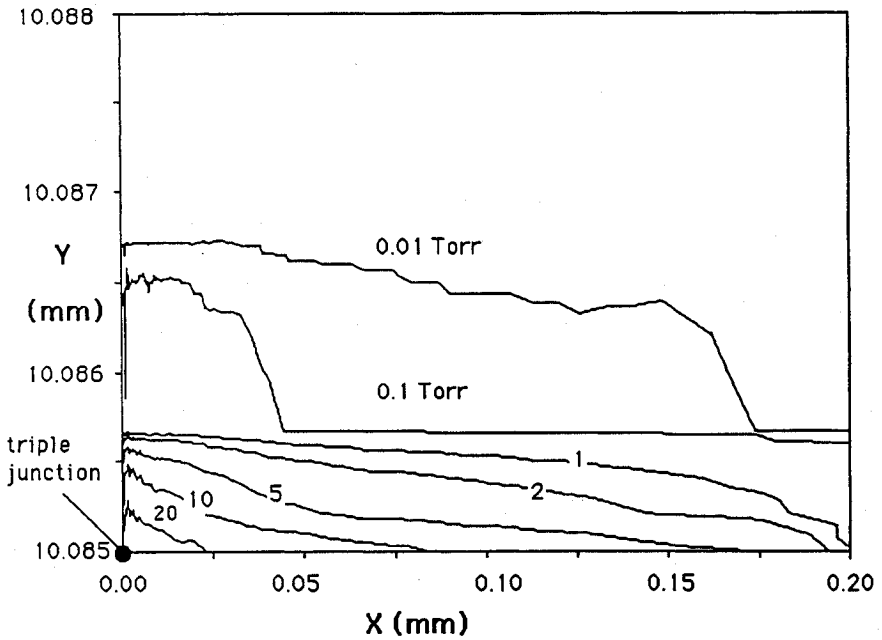

Fig. 8 Neutral density (Torr) due to EID at $T = 300$ K at $t = 766.0$ ns (1 ns after the intensive desorption begins) with $Q = 5 \times 10^{-19}$ m^2 and $N_n(t = 0) = 10^{19}$ m^2. It should be noted that X and Y scales are different in the figure.

D. Neutral Desorption

Because of the intense electron incident current on the dielectric side surface, a significant amount of neutral gas can be desorbed from the surface. A dense, very localized neutral cloud emerges over the dielectric surface. In this paper, we are interested in the neutral density of this cloud when an arc is just initiated. The onset of arcing is a very fast process whose time scale is much shorter than a microsecond. The heating during such a short time scale is insufficient to cause massive outgassing due to thermal desorption from the dielectric surface. The thermal desorption from the conductor surface due to the joule heating at the emission site is also negligible in this short time scale. Therefore, it is very likely that electron impact desorption (EID)[14] determines the density. The desorption flux due to EID, Γ_{EID}, is given by

$$\Gamma_{EID} = N_n Q_{EID} \frac{j_e}{e} \tag{13}$$

Typically, Q_{EID} is from 10^{-19} m^2 to 10^{-24} m^2, depending on the binding state of the adsorbate.[14] The rate of change of the surface neutral density N_n is given by $dN_n/dt = -\Gamma_{EID}$. Since we know the incident electron flux, we can calculate the desorption flux and the resulting neutral density n_n with some assumptions about the initial surface neutral density per unit area N_n and the EID cross section Q_{EID}.

For the desorbing species, we choose H_2O based on several experimental observations that water is involved in arcing onset.[15,16] We assume that the neutrals are desorbed with the same temperature as the surface (300 K) and a cosine angular distribution. The temperature 300 K is the condition where the SFU ground experiment was done. One difficulty associated with the present modeling of desorption process is that we have no knowledge about the exact surface conditions of the dielectric. Therefore, in the present study the parameters of EID, such as N_n and Q_{EID}, are treated as variables.

In Fig. 8, we show the neutral density desorbed for the case shown in Fig. 5. It should be noted that the x and y scales in the figure are different. The length of the side surface is 0.19 mm in the x direction. The field emission site lies on the conductor surface from $Y = 10.085$ mm to $Y = 10.088$ mm. In this case, the initial EID yield $N_n(t = 0)Q_{EID}$ has been assumed to be five gas molecules per incident electron. The initial surface gas density is assumed to be a monolayer $N_n = 10^{19}$ m^{-2}, and the cross section is assumed to be $Q_{EID} = 5 \times 10^{-19}$ m^2. The EID yield of 5 molecules/electron corresponds to the maximum yield found in experimental studies.[14,17] Therefore, the neutral gas density shown here can be regarded as the upper-bound on the neutral density as the result of EID for the given incident electron current density to the surface.

To obtain the result shown in Fig. 8, we have used a Direct Simulation Monte Carlo (DSMC) code. However, the mean free path of neutral-neutral collision is a few microns at its minimum and the neutrals behave as a free molecular flow. In this case, the DSMC code becomes just a free molecular flow code which follows particle trajectories. Nevertheless, the code has been used because it can handle a complex physical boundary. Once a neutral particle reaches any physical boundary, we have assumed that it is reflected by reversing the normal velocity to the surface while keeping the tangential velocity the same.

The density gradient seen in Fig. 8 is due to the speed distribution of the desorbed neutrals and the nonuniformity of the neutral desorption flux at the dielectric side surface. As time goes by, the high-pressure zone $\mathcal{O}(1 \sim 10$ Torr) in Fig. 8 moves upward as long as the high electron incident current to the dielectric surface continues, and electrons travel mostly through the high-pressure environment. The scale length for the electron paths is given by the thickness of the dielectric ($\simeq 200$ μm). Then, the product of the pressure and length is less than the Paschen minimum $(pd)_{\min} \sim \mathcal{O}(1$ Torr $\cdot$ cm), where the breakdown voltage goes up very sharply because the ionization collision mean free path becomes comparable or longer than the length d. The fact that arcing occurs at a few hundred volts in experiments indicates that if arcing onset is due to breakdown of the desorbed neutrals, the gas breakdown must be due to a mechanism other than a classical Townsend breakdown.[8]

III. Semivacuum Breakdown of Outgassed Neutral Cloud

A. MC-PIC Simulation

In this section, we conduct computer particle simulations using a two-dimensional MC-PIC code. The details of the one-dimensional MC-PIC code are given in Ref. 2. The objective of the two-dimensional MC-PIC simulation is to demonstrate by computer simulation that the arcing onset occurs even at the small value of pd shown in the previous section and verify the arcing onset model proposed in earlier work.[1-3] The MC-PIC code has been chosen because it can handle charged particle-neutral collisions and charged particle motion self-consistently along with the space charge density. The same

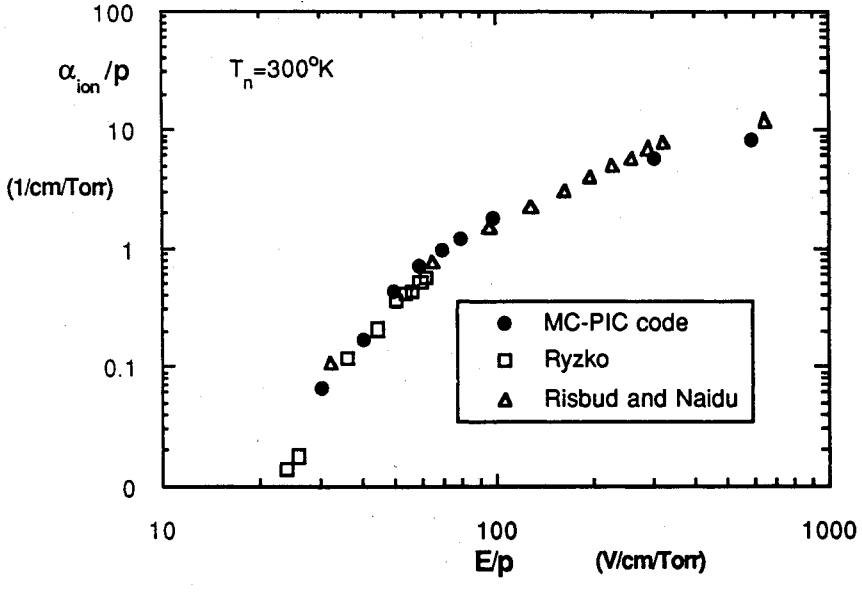

Fig. 9 Townsend ionization coefficient of water vapor calculated by the MC-PIC code and the experimental data of Ryżko[18] and Risbud and Naidu.[19]

parameters are used as in Sec. II and we use the results obtained in that section as the initial conditions for the simulations of this section.

In the MC-PIC simulation, we consider five species of charged particles. They are electrons, H_2O^+, Ar^+, H^-, and H^+. H_2O^+ is the result of electron-neutral collisional ionization, and Ar^+ is used as the background plasma species. The negative hydrogen ion is the result of dissociative attachment of water vapor. The positive hydrogen ion is the result of ionic desorption due to EID from the dielectric surface. For simplicity, we fixed the ionic EID yield at 10^{-4} (ion/electron)for all of the cases. The real charge-to-mass ratios are used for all of the species, unless noted otherwise. They are $[(q_i/m_i)_{H_2O^+}]/[|q_e/m_e|] = 3.05 \times 10^{-5}$ for H_2O^+, 1.37×10^{-5} for argon, 5.45×10^{-4} for positive hydrogen, and 5.44×10^{-4} for negative hydrogen. The collision cross-section data used in the simulation is discussed in Ref. 13. Figure 9 shows the Townsend ionization coefficient of water vapor calculated by the one-dimensional MC-PIC code. The details of the calculation are given in Ref. 13. The experimental data of Ryżko[18] and Risbud and Naidu[19] are also shown. The MC-PIC code can simulate the charged particle-neutral collision processes with very good quantitative accuracy.

We show the total electron emission current from the emission site in Fig. 10. The simulation is started from $t = 766$ ns with the neutral densities shown in Fig. 10. The neutral density is updated every 1 ns by running the DSMC code independently with the self-consistent neutral desorption flux given by Eq. (13). In Fig. 10, it is shown that once neutrals appear in the domain, the electron current begins to increase exponentially. We have checked the number of ions arriving at the conductor surface, which is far smaller than the number of electrons emitted. Therefore, the current increase shown in the figure is not a classical Townsend discharge, where more ion current is necessary than electron emission current from the cathode. The breakdown can be explained by the BKG model where the current increase is due to the field enhancement by positive space charge resulting from ionization of neutrals.

As the bulk of positive ions approaches the conductor surface, the electric field is enhanced by the $\delta E^+ = C^+ j_i$. Initially, the emission current density from the conductor is the space-charge-limited current j_{ec}^*. Because of the field enhancement of δE^+, the resulting electron emission current j_{ec}^+ is given by

$$j_{ec}^+ = A'\beta^2(E_{c.o.} + \delta E)^2 \exp\left[-\frac{B}{\beta(E_{c.o.} + \delta E)}\right]$$

$$\simeq A'\beta^2 E_{c.o.}^2 \exp\left(-\frac{B}{\beta E_{c.o.}}\right) \exp\left(\frac{B}{E_{c.o.}} \frac{\delta E^+}{\beta E_{c.o.}}\right)$$

$$= j_{ec}^* \exp\left(\frac{B}{\beta E_{c.o.}} \frac{C^+ j_i}{E_{c.o.}}\right)$$

where the assumption that the initial field $E_{c.o.}$ is much larger than E^+ has been used.The initial current j_{ec}^* is increased by a factor of $\exp[(B/\beta E_{c.o.})(C^+ j_i/E_{c.o.})]$. Therefore, the current j_i does not have to be larger than the initial electron current j_{ec}^* to cause the gas breakdown.

When the ion current density j_i exceeds a certain value, the positive space charge outweighs the increase of negative charge due to the emission current increase, because an ion moves very slowly thereby giving a much stronger space charge effect than an electron. Consequently, the emission current increases without limitation due to the negative space charge; this can therefore be regarded as arcing onset. As we can see from Fig. 10, the arcing onset is a very fast process of the order of a nanosecond.

We now calculate a breakdown curve using the MC-PIC code. For simplicity, we artificially set the density of the neutral cloud uniform in space and constant in time. We lay down a neutral cloud of 10-μm height over the dielectric side surface. The breakdown voltage is now calculated as a function of this neutral density. The boundaries of the artificial neutral cloud are given by the dielectric side surface, conductor surface, a line parallel to the side surface separated by 10 μm, and a line extended from the coverglass front surface by 10 μm. Inside the boundary, the neutral density is assumed to be constant and uniform with some value, and outside the boundary the ambient value $p = 4 \times 10^{-4}$ Torr is assumed. The height of the cloud has been determined from the numerical observation that most of the electrons lie within 10 μm from the surface. The neutral pressure inside the cloud is varied assuming $T_n = 300$ K for a given bias voltage, to find

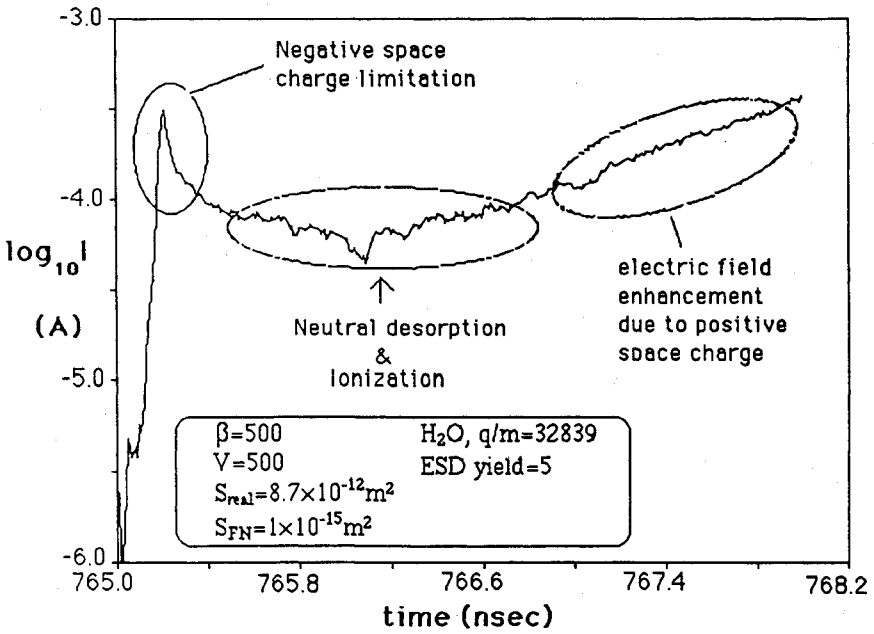

Fig. 10 Electron emission current from conductor surface for the initial EID yield = 5. The neutral density shown in Fig. 8 is assigned to each grid cell at $t = 766$ ns and the neutral density is renewed at every 1 ns using the self-consistent electron incident current and the desorption flux.

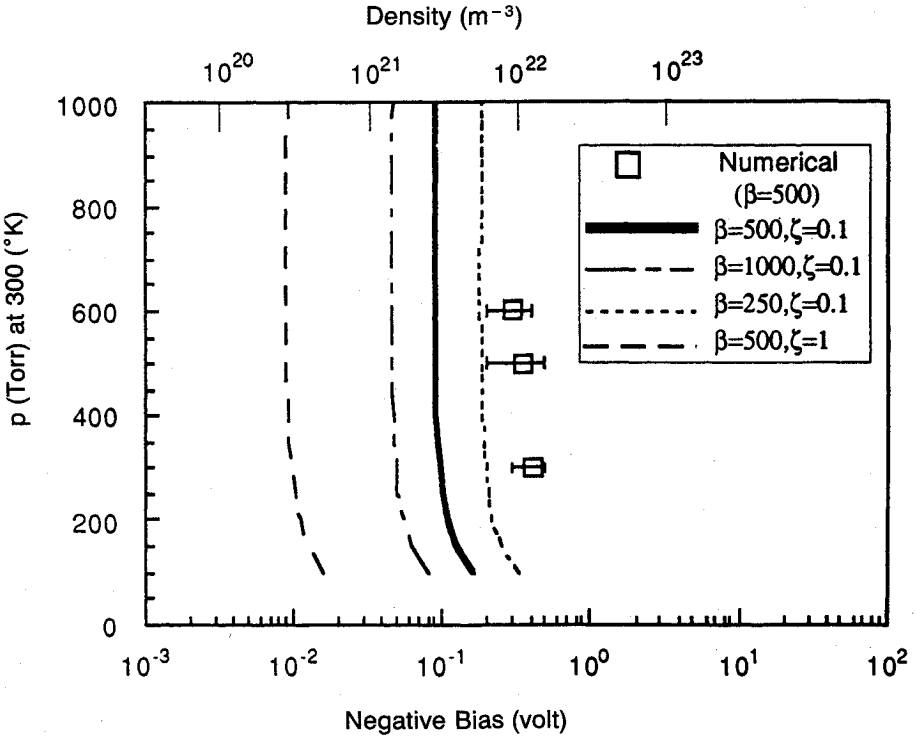

Fig. 11 Breakdown condition of water vapor desorbed from the dielectric side surface.

the pressure which gives arcing onset. The arcing onset is judged by whether the emission current exceeds the peak value without ionization, such as the one shown in Fig. 5. We use a charge to mass ratio 0.01 for H_2O^+, in order to reduce the CPU time while still keeping the ion and electron time scales different.

The results for three bias voltages with $\beta = 500$ are shown in Fig. 11. The error bars in the figure indicate that at the left of the error bar we saw no arcing onset and at the right we saw arcing onset. The breakdown voltages shown in the figure are much lower than the Paschen breakdown voltage whose minimum is 2000 V for H_2O vapor.[20]

B. Breakdown Condition and Critical EID Yield

We now formulate a parametric formula of the breakdown neutral density. This is the modification of the one-dimensional analysis whose details are given in Ref. 2. In the present paper, we show only the differences from the previous work. The ion current density in front of the emission site is given by

$$j_i = \zeta[\exp(n_n \sigma_{ion} d) - 1] j_{e0} \simeq \zeta(n_n \sigma_{ion} d) j_{ec}^* \tag{14}$$

where ζ is the fraction of the ion current which contributes to the field enhancement at the emission site, because not all of the ions come near the emission site due to the deflection of their paths by the field component E_y. The initial current density j_{e0} is the current from the cathode before any ionization begins and equal to j_{ec}^* for the present case. In Ref. 2, one-dimensional equations were solved analytically to obtain the field enhancement factor C^+. For the present case, the factor C^+ is modified to

$$C^+ = 0.8 \frac{d_2}{\epsilon_o} \left(\frac{m_i}{2e}\right)^{1/2} \frac{1}{|V_{ad}|^{1/2}} \tag{15}$$

The differences from the previous one-dimensional analysis in Ref. 2 are only ζ, and the use of V_{ad} and d_2 in Eq. (15).

The one-dimensional breakdown condition, Eq. (22) of Ref. 2, is now modified to

$$n_n \geq 0.46 \frac{\epsilon_o V_{ad}^{1/2}}{\zeta \sigma_{ion}(d_1 + d_2) d_2 A' \beta B} \left(\frac{2e}{m_i}\right)^{1/2} \exp\left(\frac{B}{\beta E_{c.o.}}\right) \tag{16}$$

where the initial cathode (conductor) field $E_{c.o.}$ and the factor ζ must be calculated numerically. Using Eqs. (2) and (9), we can calculate $E_{c.o.}$ which gives j_{ec}^* by solving the following equation:

$$A'(\beta E_{c.o.})^2 \exp\left(-\frac{B}{\beta E_{c.o.}}\right) = 1.05 \epsilon_o \sqrt{\frac{2e}{m_e}} \frac{\sqrt{E_{se}}}{\sqrt{S_{real} d}} |V| \tag{17}$$

for a given bias voltage V. We approximate the ion concentration factor by $\zeta = 0.1$ from the results of the PIC simulations. The breakdown curve calculated by Eq. (16) is shown in Fig. 11. The result agrees well with the MC-PIC simulation results. For comparison, the curve for $\zeta = 1$ is also shown to show how this parameter affects the result, which corresponds to the case where every returning ion contributes to the field enhancement at the emission site.

In Fig. 11, the sharp increase of the breakdown voltage is due to the fact that the current $j_{e0}(= j_{ec}^*)$ is limited by negative electron space charge before any ionization starts. Then, the current j_{e0} is not an exponential, but a linear function of V as shown in Fig. 7, and the neutral density threshold for the onset of arcing is almost constant for the voltages higher than a few hundred volts. The breakdown density is very insensitive to the field enhancement factor. Therefore, once EFEE charging occurs, arcing onset follows when a certain amount of neutral gas ($10^{21} \sim 10^{22}$ m^{-3}) is desorbed from the surface irrespective of β.

The density of the neutral cloud produced at each bias voltage depends linearly on the EID yield $N_n Q$ and the incident electron current density j_e. Since the neutral desorption flux can be approximated by a free molecular flow, the average neutral density is estimated by

$$n_n = \frac{N_n Q_{EID}}{\frac{1}{4}\bar{c}} \left(\frac{j_e^*}{e}\right) \tag{18}$$

where $\bar{c} = \sqrt{(8\kappa T_n)/(\pi m_n)}$. In the above equation, the surface neutral density N_n can be assumed constant in time, because the time scale of the change of N_n given by $Q_{EID} j_e / e$ from Eq. (13) is an order of a microsecond or more and much longer than the time scale of interest here. Substituting Eq. (12) into

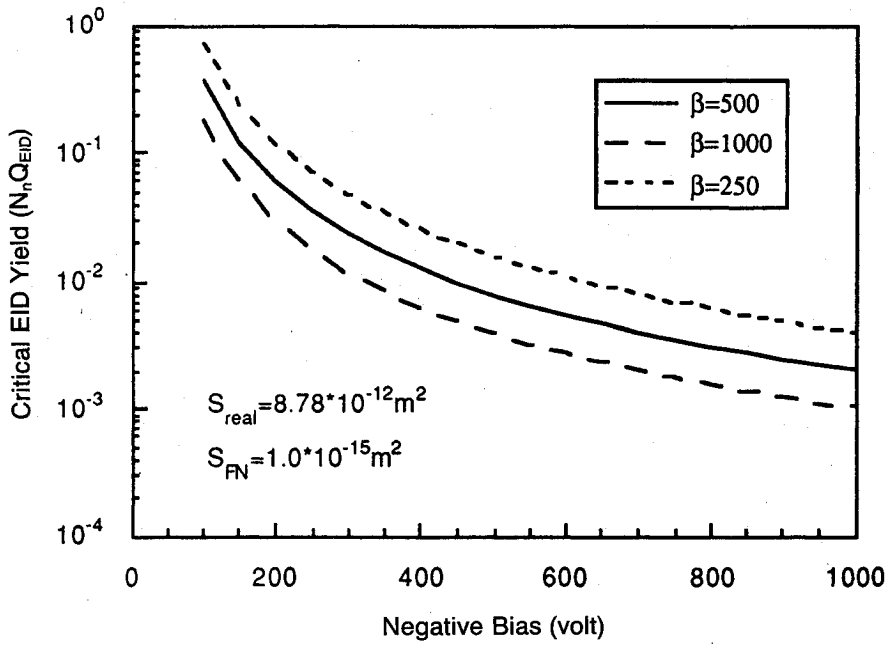

Fig. 12 Critical EID yield for the arcing onset for $\beta = 500$, 1000, and 250.

j_e^*, the neutral density n_n is given by

$$n_n = 2.08\frac{N_nQ_{EID}}{\bar{c}}\frac{\epsilon_o}{e\sqrt{m_e}}\frac{\sqrt{2e}}{E_{sel}d^2}|V|^2 \tag{19}$$

With this expression and Eqs. (16) and (17), we can determine the critical EID yield for the arcing onset for a given bias voltage V.

Figure 12 shows the critical EID yields N_nQ_{EID} calculated by substituting Eqs. (17) and (19) into Eq. (16) for three different βs. For the different βs the result changes little. If an EID yield is higher than the values shown in the figure, arcing occurs. For bias voltages $|V|<500$ V, the critical EID yield is from 0.01 to 1. It goes up sharply as the bias voltage becomes less than 150 V. An EID yield of the order of 10^{-2} is usually seen in the literature of EID yield measurement, and $N_nQ_{EID} \sim \mathcal{O}(1)$ corresponds to the upper bound on the values seen in the literature.[14] Therefore, once the EFEE current starts to increase as shown in Fig. 2, arcing occurs easily at the bias voltage $|V|>150$ V. However, it becomes increasingly difficult to have arcing onset as the voltage goes below 150 V, which is a common experimental observation. Another common experimental fact of high-voltage solar array arcing is that the arcing rate decreases as the experiment continues. This can be also attributed to the decrease of EID yield (mostly N_n) due to successive outgassing by arcing.

Table 1 Breakdown neutral density and critical EID yield calculated by Eqs. (16) and (19) for various sets of parameters at $\beta = 500$ and $\zeta = 0.1$

E_{se}, eV	S_{real}, $\times 10^{-11}$ m^2	S_{FN}, $\times 10^{-15}$ m^2	$\|V\|$, V	n_n, $\times 10^{21}$ m^{-3}	N_nQ_{EID}
2	100	1	100	84	14
2	1	1	100	5.8	0.98
2	0.01	1	100	0.42	0.071
2	1	100	100	3.2	0.54
2	1	0.01	100	13	2.2
0.5	1	1	100	11	3.5
4	1	1	100	4.3	0.52
2	100	1	500	49	0.33
2	1	1	500	3.2	0.022
2	0.01	1	500	0.23	0.0015
2	1	100	500	1.7	0.011
2	1	0.01	500	8.0	0.054
0.5	1	1	500	5.8	0.078
4	1	1	500	2.4	0.12

In Table 1, we summarize the breakdown neutral density and the critical EID yield for different sets of the parameters. For most cases, the breakdown density is from 10^{21} m^{-3} to 10^{22} m^{-3} showing the insensitiveness of these parameters to the results. The critical EID yields are mostly less than 0.1 at $|V| = 500$ V making it easy to arc. However, at $|V| = 100$ V, the critical yields are so high that the onset of arcing is unlikely.

IV. Arc Rate

We now apply the result in the previous section to interpret some of the experimental observations regarding arcing rate. Figure 13 shows the arc rate against the sample temperature, which was measured by Kuninaka[3] in the SFU-HVSA ground experiment. The data was taken at a plasma density of 1.1×10^{11} m^{-3} and a background pressure of 4×10^{-4} Torr. In Ref. 3, whenever the electric field at the triple junction showed a runaway, it was regarded as arcing onset. This assumption resulted in the upper bound on the arcing rate and could not provide a theoretical prediction on the temperature dependence. In the present paper, we add one more condition to determine whether the arcing onset is possible or not by taking into account the semivacuum breakdown condition. We calculate the outgassed neutral density by Eq. (19) at each EFEE site and compare it to the critical neutral density, n_{nc}. The arc interval is equal to the charging time of the EFEE site which gives the shortest charging time among the sites where $n_n > n_{nc}$, that is,

$$\tau_{arc} = \min[\tau_{chrg}(n_n > n_{nc})] \tag{20}$$

The details of the procedure to calculate the charging time τ_{chrg} is given in Ref. 3.

For a given sample temperature, we calculate the adsorbed neutral density N_n^* given by the balance between the thermal desorption flux which is

$$\Gamma_{TSD} = k_1^0 N_n^* \exp[-(E_d/\kappa T_s)]$$

and the adsorption flux $n_{na}(\bar{c}/4)s$ with s approximated by $s = 1 - N_n^*/N_{no}$. Equating both the fluxes, we obtain

$$N_n^* = \frac{n_{na}(\bar{c}/4)}{n_{na}(\bar{c}/4) + \kappa_1^0 N_{no}\exp[-(E_d/\kappa T_s)]}N_{no} \tag{21}$$

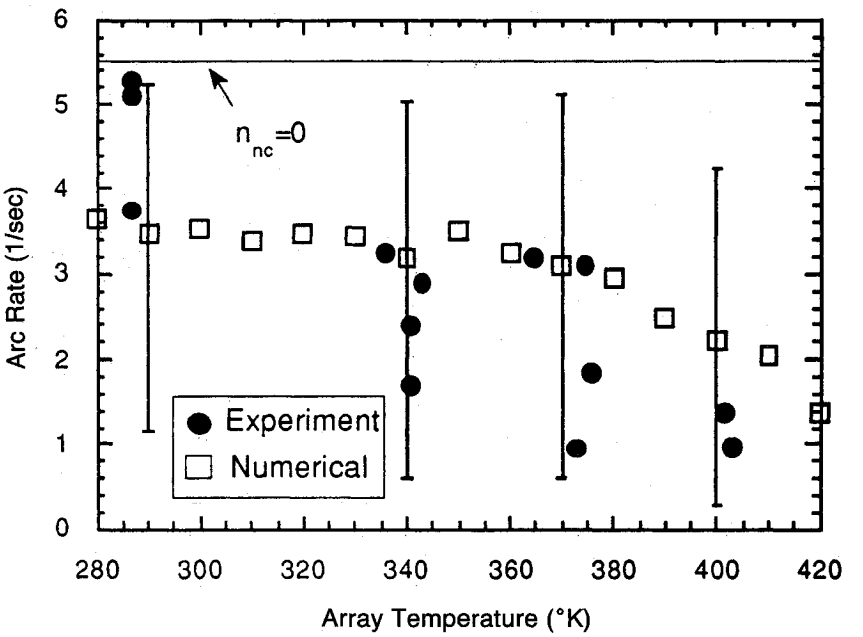

Fig. 13 Arc rate against array temperature for density of $n_e = 1.1 \times 10^{12}$ m^{-3} and voltage of 500 V. The vertical bars denote the region within which a calculated arc rate falls with a probability of 0.8. The horizontal line indicates the arcing rate for $n_{nc} \to 0$, giving the upper bound on the arcing rate.

This neutral density is adsorbed on the dielectric surface before the intensive outgassing due to electron impact begins. Since we do not know the details of the surface conditions, we assume an EID cross section Q_{EID} which varies within some reasonable range at each emission site. We choose Q_{EID} from a distribution function, where $\log_{10} Q_{EID}$ is uniformly distributed from $Q_{EID} = 1 \times 10^{-19}$ to 1×10^{-23} in square meters. The upper bound of Q_{EID} corresponds to the gas particle-electron collision. The lower bound corresponds to an EID yield of 0.0001 for a monolayer $N_{n0} = 10^{19}$ m^{-2}. The effect of the range of Q_{EID} is discussed later. From Table 4.5 of Ref. 21, we take $E_d = 0.9$ eV. The other parameters assumed are $n_{na} = 1.3 \times 10^{19}$ m^{-3} (4×10^{-4} Torr at 300 K), $\bar{c} = \sqrt{(8\kappa T_s)/(\pi m_n)}$ with $m_n = 2.99 \times 10^{-26}$ kg (water vapor), and $k_1^0 = 10^{13}$ s. The secondary electron properties E_{se} and E_{se1} are chosen to be $E_{se} = 2$ eV and $E_{se1} = 7.6$ eV. From Fig. 11, we deduce the critical neutral density for the arcing onset $n_{nc} = 6.4 \times 10^{21}$ m^{-3}.

In Fig. 13, the average values of the calculated arc rates are plotted against the sample temperature. The average values are calculated from 100 data samples at each temperature. The arc rate is a random variable determined by the combination of the physical parameters and the experimental results indeed show a scatter of the data. The number of experimental data points is insufficient to derive any statistical distribution from them. As an alternative to judge the agreement between the experiment and theory, we make a significance test of the theoretical model by seeing whether the experimental data lie in probable ranges of the theoretical predictions. We denote an acceptance region of the model with a significance of 0.2 by the vertical bars attached to some of the numerical results in Fig. 13. The acceptance region is defined by the range within which a calculated arc rate falls with a probability of 0.8 (for example, see Ref. 22). If an experimental value is outside the region, it is an improbable event and the theoretical model to describe the experimental data can be rejected. However, for the present case, all of the experimental data lie within the acceptance region and our theoretical model is accepted.

The three most important parameters for determining the arc rate as a function of temperature are the range of Q_{EID}, the ambient plasma density, and the desorption energy E_d. The range of Q_{EID} determines the scatter of the numerical data. The larger we take the range, the larger scatter we get. The upper bound of the arc rate at $n_{nc} = 0$ is determined by the ambient ion density.[3] The desorption energy E_d determines the temperature where the arc rate begins to decrease. The probability that the arcing onset does not occur is inversely proportional to the adsorbed neutral density N_n^*, which has an exponential dependence on the surface temperature. The arc rate begins to drop when the flux $k_1^0 N_{no} \exp(-E_d/\kappa T_s)$ becomes comparable to the flux $n_{na}\bar{c}/4$ in the denominator of Eq. (21) and this occurs at $T_s \simeq 360$ K for the present case.

V. Conclusions

In the past decade, several theoretical models have been proposed for the onset mechanism of high-voltage solar array arcing. However, these models have been limited to simple parametric studies for the discharge criteria. No attempt has been made by experiment nor by computer simulation to reproduce the arcing onset based on the theoretical models. In the present paper, a computer simulation has been undertaken to verify the arcing onset model proposed in the earlier work[1-3] by reproducing the arcing onset phenomena in a self-consistent computer particle simulation with a reasonable set of the parameters. In this final section, we conclude this paper by summarizing the new findings found in this paper and suggesting future work.

We have found that the rapid increase of the enhanced field electron emission (EFEE) current observed in Ref. 1 is limited by the negative space charge of electrons. A sheet of electrons covering the dielectric side surface cancels the positive space charge stored beforehand by secondary electron emission. The EFEE current becomes quasisteady on the time scale of nanosecond and an analytical expression for the space-charge-limited current has been obtained. The current level is not high enough to attribute this to the arc current observed in experiments.

However, at the same time, there is a strong electron incident current on the dielectric side surface. The analytical expression for the electron incident current has been obtained. It has been shown that the electron impact desorption (EID) flux resulted from the electron impact on the dielectric surface can be regarded as a free molecular flow in the region of interest. The calculation of the neutral flow has shown that the neutral environment over the surface is characterized as "semivacuum," where the ionization collision mean free path is longer than the characteristic scale length of the region, namely, the dielectric thickness.

With the self-consistent desorption flux, two-dimensional Monte Carlo-Particle in Cell (MC-PIC) simulations have shown that arcing onset occurs as the result of field enhancement by the positive space charge of ions, not as a classical Townsend discharge. Using the analytical expressions for the space-charge-limited current densities and modifying the one-dimensional breakdown condition of Ref. 2 to the two-dimensional condition, a parametric formula for the breakdown condition has been obtained. The breakdown voltage increases very sharply, giving almost constant breakdown neutral density for the voltage of interest (>100 V). The critical EID yield for the arcing onset has been also calculated. The critical EID yield increases sharply at a bias voltage $|V|$ less than 150 V giving an explanation of common experimental observations that the arcing onset becomes increasingly difficult as the voltage goes below 150 V. The breakdown condition has been applied to calculate the arc rate dependence on the array temperature observed by Kuninaka[3] and a good agreement with the experimental data has been obtained.

Future work includes study of other possible arcing onset mechanism such as dielectric breakdown. An experimental study to characterize the surface condition of the dielectric material is also underway.

Acknowledgment

The authors would like to thank H. Kuninaka for providing the experimental data for the arcing rate. This research was supported by the Air Force Office of Scientific Research under Grant AFOSR-87-0340.

References

[1]Cho, M., and Hastings, D. E., "Dielectric Charging Processes and Arcing Rates of High-Voltage Solar Arrays," *Journal of Spacecraft and Rockets,* Vol. 28, No. 6, 1991, pp. 698–706.

[2]Cho, M., and Hastings, D. E., "An Analytical and Particle Simulation Study of Localized Semivacuum Gas Breakdown Phenomena on High Voltage Surfaces in Low Earth Orbit," *Physics of Fluid B,* Vol. 4, No. 8, 1992, pp. 2614–2625.

[3]Hastings, D. E., Cho, M., and Kuninaka, H., "The Arcing Rate for a High Voltage Solar Array: Theory, Experiment and Predictions," *Journal of Spacecraft and Rockets,* Vol. 29, No. 4, 1992, pp. 538–554.

[4]Grier, N. T., "Plasma Interaction Experiment II (PIX II): Laboratory and Flight Results," *Spacecraft Environmental Interaction Technology-1983,* NASA CP-2336, March, 1983, pp. 333–347.

[5]Hastings, D. E., Weyl, G., and Kaufman, D., "A Simple Model for the Threshold Voltage for Arcing on Negatively Biased High Voltage Solar Array," *Journal of Spacecraft and Rockets,* Vol. 27, No. 4, 1990, pp. 539–544.

[6]Thieman, H., Schunk, R. W., and Bogus, K., "Where do Negatively Biased Solar Arrays Arc?," *Journal of Spacecraft and Rockets,* Vol. 27, No. 4, 1991, pp. 563–565.

[7]Parks, D. E., Jongeward, G. A., Katz, I., and Davis, V. A., "Threshold-Determining Mechanism for Discharges in High-Voltage Solar Arrays," *Journal of Spacecraft and Rockets,* Vol. 24, No. 4, 1987, pp. 367–371.

[8]Howatson, A. M., *An Introduction to Gas Discharge*, Pergamon Press, Oxford, 1965, chap. 3.

[9]Boyle, W. S., Kisliuk, P., and Germer, L. H., "Electrical Breakdown in High Vacuum," *Journal of Applied Physics,* Vol. 26, No. 6, 1955, pp. 720–725, 1955.

[10]Chaky, R. C., Nonnast, J. H., and Enoch, J., "Numerical Simulation of Sheath Structure and Current-Voltage Characteristics of a Conductor-Dielectric Disk in a Plasma," *Journal of Applied Physics,* Vol. 52, No. 12, 1981, pp. 7092–7098.

[11]Latham, R. V., *High Voltage Vacuum Insulation,* Academic, New York, 1981.

[12]Pillai, A. S., and Hackam, R., "Surface Flashover of Solid Dielectric in Vacuum," *Journal of Applied Physics,* Vol. 53, No. 4, 1982, pp. 2983–2987.

[13]Cho, M., "Arcing on High-Voltage Solar Arrays in Low Earth Orbit: Theory and Computer Particle Simulation," Ph.D. Thesis, Massachusetts Inst. of Technology, Cambridge, MA, Feb. 1992.

[14]Drinkwine, M. J., and Lichtman, D., "Electron Stimulated Desorption: a Critical Review," *Progress in Surface Science,* Vol. 8, No. 3, 1977, pp. 123–142.

[15]Upschulte, B. L., Weyle, G. M., Marinelli, W. J., Aifer, E., Hastings, D. E., and Snyder, D., "Significant Reduction in Arc Frequency of Negatively Biased Solar Cells: Observations, Diagnostics, and Mitigation Techniques," *SPRAT Conference,* Cleveland, OH, May 1990; also AIAA Paper 92-0578, Jan. 1992.

[16]Merryman, S. A., Bandy, A. J., and Gordon, L. B., "The Breakdown Characteristic of Outgassing Dominated Vacuum Regions," *Proceedings of the 23rd Intersociety Energy Conversion Engineering Conference,* ASME, New York, 1988, pp. 763–765.

[17]McCracken, G. M., Barton, R. S., and Dillon, W., "Electron-Induced Desorption of Gas from Stainless-Steel Surface," *Nuovo Cimento Supplemental,* Vol. 5, Jan. 1967, pp. 146–152.

[18]Ryżko, H., "Ionization, Attachment, and Drift Velocity of Electrons in Water Vapor and Dry Air," *Arkiv för Fysik,* Vol. 32, No. 1, 1966, pp. 1–18.

[19]Risbud, A. V., and Naidu, M. S., " Ionization and Attachment in Water Vapor and Ammonia," *Journal de Physique Colloq,* Vol. 40, No. 7, 1979, pp. c77–c78.

[20]Hackam, R., "Breakdown Potential of Water Vapor between Plane Parallel Electrodes," *Journal of Physics D: Applied Physics,* Vol. 4, No. 8, 1971, pp. 1134–1139.

[21]Holland, L., *The Properties of Glass Surfaces,* Chapman Hall Ltd., London, 1964, chap. 4.

[22]Drake, A. W., *Fundamentals of Applied Probability Theory,* McGraw-Hill, New York, 1967, Chap. 7.

Antoni K. Jakubowski
Associate Editor